

Article

Ultrasound-Assisted 1,3-Dipolar Cycloadditions Reaction Utilizing Ni-Mg-Fe LDH: A Green and Sustainable Perspective

Mohamed Abdel Salam ¹, Eman Saleem Imdadulhaq ¹, Abeer Nasser Al-Romaizan ¹, Tamer S. Saleh ^{2,*}
and Mohamed Mokhtar M. Mostafa ^{1,*}

¹ Chemistry Department, Faculty of Science, King Abdulaziz University, P.O. Box 80203, Jeddah 21589, Saudi Arabia

² Chemistry Department, College of Science, University of Jeddah, P.O. Box 80329, Jeddah 21589, Saudi Arabia

* Correspondence: tssayed@uj.edu.sa (T.S.S.); mmoustafa@kau.edu.sa (M.M.M.M.)

Abstract: Ultrasound-assisted synthesis of novel pyrazoles using Ni-Mg-Fe LDH as a catalyst in cyclopentyl methyl ether (CPME) is introduced. Different LDHs were tested as a catalyst for the synthesis of pyrazoles via a 1,3-dipolar cycloaddition reaction. Among them, Ni-Mg-Fe LDH was the superior catalyst for this reaction. This protocol offered high yields, a short reaction time, and a green solvent, and with the reuse of this catalyst six times with the same activity, it could be regarded as an ecofriendly, greener process. The NiMgFe LDH catalyst with the smallest particle size (29 nm) and largest surface area showed its superior efficacy for the 1,3 dipolar cycloaddition reaction and can be successfully used in up to six catalytic cycles with little loss of catalytic activity. A plausible mechanism for this reaction over the Ni-Mg-Fe LDH is proposed.

Keywords: layered double hydroxide; pyrazole; 1,3-dipolar cycloaddition reaction; green chemistry; ultrasonic irradiation; cyclopentyl methyl ether



Citation: Salam, M.A.; Imdadulhaq, E.S.; Al-Romaizan, A.N.; Saleh, T.S.; Mostafa, M.M.M. Ultrasound-Assisted 1,3-Dipolar Cycloadditions Reaction Utilizing Ni-Mg-Fe LDH: A Green and Sustainable Perspective. *Catalysts* **2023**, *13*, 650. <https://doi.org/10.3390/catal13040650>

Academic Editor: Fernando P. Cossio

Received: 6 February 2023

Revised: 10 March 2023

Accepted: 20 March 2023

Published: 25 March 2023



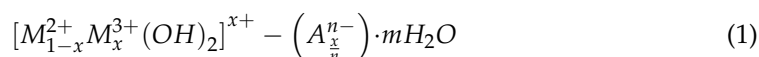
Copyright: © 2023 by the authors. Licensee MDPI, Basel, Switzerland. This article is an open access article distributed under the terms and conditions of the Creative Commons Attribution (CC BY) license (<https://creativecommons.org/licenses/by/4.0/>).

1. Introduction

The pyrazole nucleus is essential in the pharmaceutical industry and represents an exciting scaffold for medicinal chemists [1–5]. Their biological activities include antimicrobial [6], antiviral [7,8], and anticancer [9–11] agents. Several FDA-approved and commercialized drugs in recent years have been derived from pyrazole derivatives (Figure 1), suggesting that this group is widely used in newly developed bioactive molecules [12]. Figure 1 shows that many synthetic pyrazole derivatives participate as anti-inflammatories in molecules, avoiding the side effects of known nonsteroid anti-inflammatory drugs (NASIDs) in which the anti-Cox2 receptor was identified to show significant analgesic and anti-inflammatory activity without ulcerogenic effect [13]. In addition, the prevalence of multi-drug-resistant microbial infections has become a global health concern. The development of effective antimicrobials with high activity and low toxicity is a continuous requirement [14]. A number of pyrazoles are capable of effective antibacterial action, such as sulfaphenazoles (Figure 1) and others containing trifluoromethyl groups (CF₃) [15]. In addition, a fused pyrazole derivative, sildenafil, has been used to treat erectile dysfunction [16]. Moreover, some pyrazole compounds, such as Acomplia (Figure 1), that are used to treat obesity have a high affinity for CB1 cannabinoid receptors [17,18]. Due to the outstanding biological and pharmacological importance of pyrazole derivatives, many methods have been developed by medicinal chemists for the creation of new pyrazole-based drugs.

These methods include the condensation of hydrazine's (or similar) nuclei with carbonyl functional group compounds, such as the reaction of amine-functionalized enamines and aryl sulfonyl hydrazine or tosylhydrazine [19], the reaction of hydrazide with 1,3-diketone [20], and the reaction of arylhydrazines with acetylenic ketones [21], as well as

dipolar additions that involve the reaction of ketone with acetyl diazoester [22], the [3 + 2] cycloaddition of dipolarophiles with structurally varied 4-methylbenzenesulfonylhydrazides [23], and many other methods [24,25], including 1,3-dipolar cycloaddition (1,3-DC) [26]. 1,3-DC is considered one of the most essential methods used to synthesize pyrazole derivatives. This depends on the reaction of nitrilimine (generated in situ by the action of the base on the hydrazonoyl halide) with α,β -unsaturated carbonyl compounds [26,27]. The main drawbacks of this method are the use of hazardous volatile organic solvents such as benzene and the use of a stoichiometric homogeneous base catalyst such as triethylamine. Recently, Saleh et al. reported [28] an ecofriendly, green protocol for synthesizing pyrazole derivatives in a solvent-free fashion utilizing a Mg-Al HT catalyst. This report considered the first protocol that avoids a hazardous organic solvent in a 1,3-dipolar cycloaddition reaction. It is noteworthy that hydrotalcite-like materials, abbreviated to HTs or layered double hydroxides (LDHs), are a class of beneficial materials for organic chemists in organic catalysis. HTs or LDHs consist of positively charged two-dimensional sheets with water and exchangeable charge-compensating anions in the interlayer region. Their general formula is [29]:



where M^{2+} and M^{3+} represent divalent and trivalent cations in the brucite-type layers, A is the interlayer anion with charge n , x is the fraction of the trivalent cation (x values in the general formula are in the range of 0.20–0.50), and m is the water of crystallization. Two essential characteristics of LDHs are necessary for organic chemists; the first is a considerable anion-exchange capacity, and a second crucial characteristic of HTs is that they behave as solid bases [30,31].

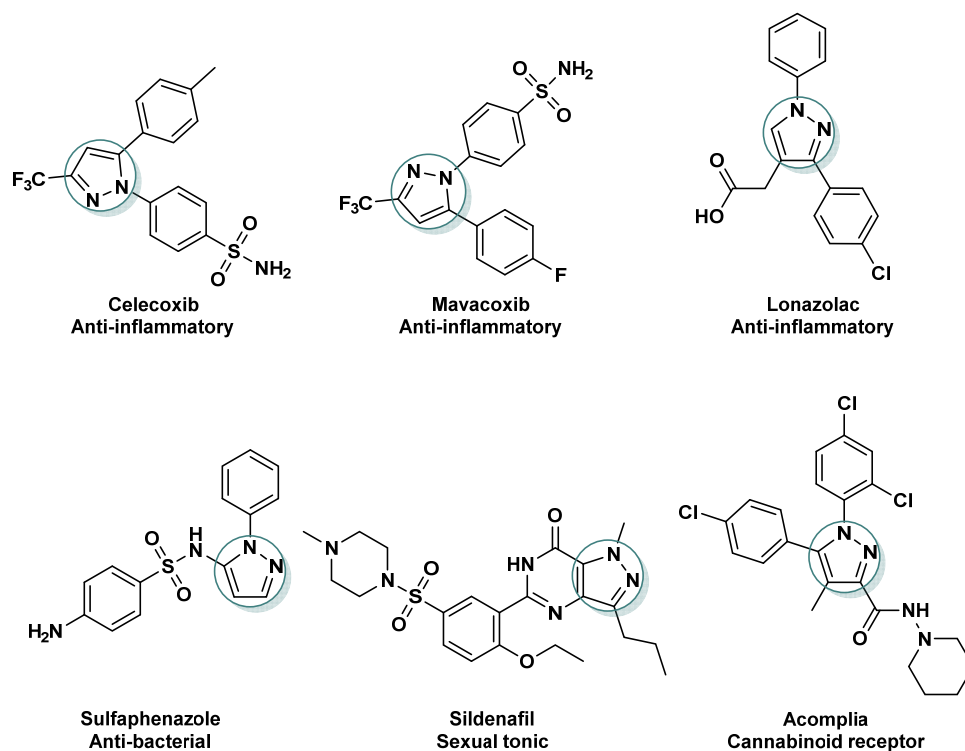


Figure 1. Several biologically active molecules containing pyrazole.

LDHs are an excellent choice for catalytic processes due to the fact of their unique basic properties. By exchanging the two- and three-valent cations in LDHs, their basicity properties become tunable [32]. The basicity of rehydrated LDHs is increased when the interlayer anion is replaced by Brönsted OH groups [33,34]. Moreover, because of their capacity to interact with atoms, ions, and molecules not only at their surface but also within the material, porous materials with a tunable pore architecture are receiving a lot

of interest [35,36]. Thus, the properties of materials (such as the external surface area, diffusivity, and basicity) that are needed for advanced applications can be significantly modified by reducing the crystallite size to the nanometer range, and downsizing the crystals has attracted much attention in recent years [37,38]. It is noteworthy that LDHs play an important role in catalytic organic synthesis in which NiAl LDHs are used for the carbon dioxide methanation reaction [39]; in addition, Mg-La LDHs present a strong basic character, achieving higher yields in organic reactions that require a strong basic catalyst [40]. However, the properties of LDHs can also be changed with the incorporation of another divalent cation in the brucite layer. Metals, such as Cu^{2+} , Ni^{2+} , Fe^{2+} , Ca^{2+} , Co^{2+} , and Zn^{2+} , among others, can be incorporated into the laminar structure, which allows for obtaining a great variety of materials with catalytic properties. Therefore, as heterogeneous catalysts, hydrotalcites conduct highly efficient processes in short reaction times. Moreover, they are easy to recover and reuse without losing much catalytic activity. Additionally, their modified structural and chemical properties make them useful catalysts for organic synthesis, including Michael's addition reactions, dehydrogenation reactions of alcohols, Knoevenagel condensations, reduction reactions, oxidations, epoxidations, and multicomponent reactions [41].

On the other hand, ultrasound has been recognized as a key technique in green and sustainable chemical processes used in laboratory to industrial applications [42–45]. With a focus on more sustainable protocols, sonochemistry has gained prominence as a technique for using sound in a broad range of frequencies and powers [45]. Even though ultrasonic activation is based on well-established cavitation principles, the first step is to know what equipment is needed and how it works. When a few parameters are taken into consideration, reproducible experiments can be carried out [46]. There are known facts that should be taken into consideration when using sonochemistry. In either a physical or chemical sense, some reactions and substrates are sensitive to sonication. In order to understand how the reaction occurs, it may be important to take a reductionist approach that simply considers either convergent or divergent results in conventional chemistry. Regardless of the mechanism, a different result under sonication does not necessarily indicate the formation of radicals or electrons; two polar mechanisms can compete with one another [46]. The most divergent results come from sono-mechanochemistry, which incorporates turbulent solvent flows at the microscale in order to cause mechanical effects, particularly in polymer chains [46]. The ultrasound techniques are usually performed for heterogeneous liquid/liquid and solid/liquid systems. Therefore, the choice of used solvent for the organic reaction in ultrasonic techniques is essential [47]. More recently, two critical reviews that used cyclopentyl methyl ether (CPME) were released [48,49] showing the advantages of CPME, including low toxicity, high boiling point, low melting point, hydrophobicity, and chemical stability, making it a good ecofriendly choice of solvent for a variety of organic reactions. Bearing in mind all of the above, as part of our program toward a nonconventional approach to the experimental setup of organic reactions [50–54], herein, we introduce a green and sustainable route for a 1,3-DC reaction utilizing a Ni-Mg-Fe LDH catalyst in CPME solvent under ultrasonic irradiation.

2. Results and Discussion

2.1. Catalyst Characterization

In the current study, Mg-Fe LDH and Ni-Mg-Fe LDH catalysts were manufactured using the coprecipitation method. A comprehensive physicochemical characterization was performed and is presented in this section. The catalytic efficiency of the synthesis of pyrazoles via a 1,3-dipolar cycloaddition reaction was tested. This selection was based on the predictable physicochemical characteristics that could be essential for improving the catalytic process under ultrasound irradiation.

2.2. Thermal Gravimetric Analysis (TGA)

Thermogravimetric analyses of all of the samples are shown in Figure 2. The thermograms of the Ni-Mg-Fe LDH and Mg-Fe LDH were analyzed to obtain information on the percentage weight loss at different temperatures. The thermal decomposition of this hydrotalcite appeared to undergo a basic four-step mechanism, common to most LDHs [55]. In the Ni-Mg-Fe LDH, they showed two stages of weight loss, while the Mg-Fe LDH thermal decomposition showed three stages. In the Ni-Mg-Fe LDH, the first range of weight loss (64–214 °C), accounting for 13.2% of the total mass, is indicative of the removal of physisorbed water and of the interlayer of water molecules (i.e., dehydration). The second range of weight loss (214–358 °C), amounting to a further ca. 14.05% of the total mass, is attributed to the removal of OH[−] groups and the decarbonation of the carbonate anions present in the interlayer space of the LDH, leading to the formation of metal oxides [55,56]. In the Mg-Fe LDH, the first range of weight loss (44–209 °C), amounting to 13.43% of the total mass, is indicative of the removal of physisorbed water and of the interlayer water molecules (i.e., dehydration). The second range of weight loss (209–452 °C), amounting to a further ca. 17.28% of the total mass, is attributed to the removal of OH[−] groups and the decarbonation of carbonate anions present in the interlayer space of the LDH, leading to the formation of metal oxides [57].

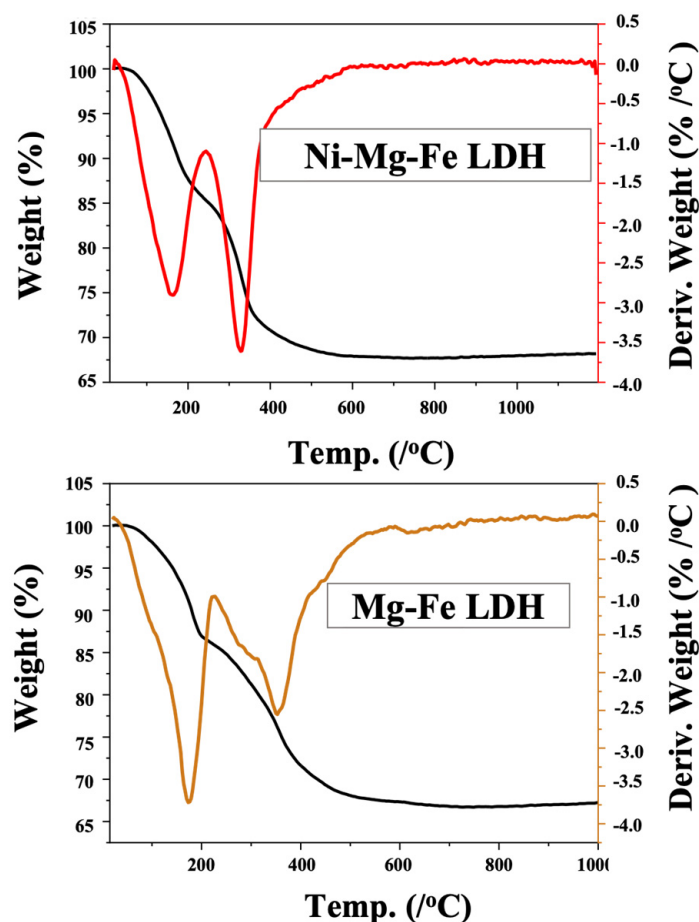


Figure 2. TGA and DTG thermograms of the Mg-Fe LDH and Ni-Mg-Fe LDH catalysts.

2.3. X-ray Diffraction (XRD)

The X-ray diffraction patterns of the Mg-Fe LDH and Ni-Mg-Fe LDH catalysts are presented in Figure 3. All samples successfully synthesized in this study were identified to a single phase of the LDH [58]. The analysis of the Mg-Fe LDH sample indicated the formation of the pyroaurite phase in which a great deal of the material was formed. From the crystallization, its characteristic diffraction peaks at 11.56°, 23.2°, 34.3°, and

38.7° corresponded to the typical basal spacings (003), (006), (009), and (015), respectively, matching well with the (PDF No. 14–0365) references [59,60]. The diffraction peaks of the Ni-Mg-Fe LDH sample corresponded to the (003), (006), (006), (012), and (113) spacings, which is equal to that of conventionally synthesized LDHs [61]. The average crystallite size was calculated by the Scherrer equation using the FWHM of the reflection plane (003) for the Mg-Fe LDH and Ni-Mg-Fe LDH, and they were equal to 32 and 29 nm, respectively.

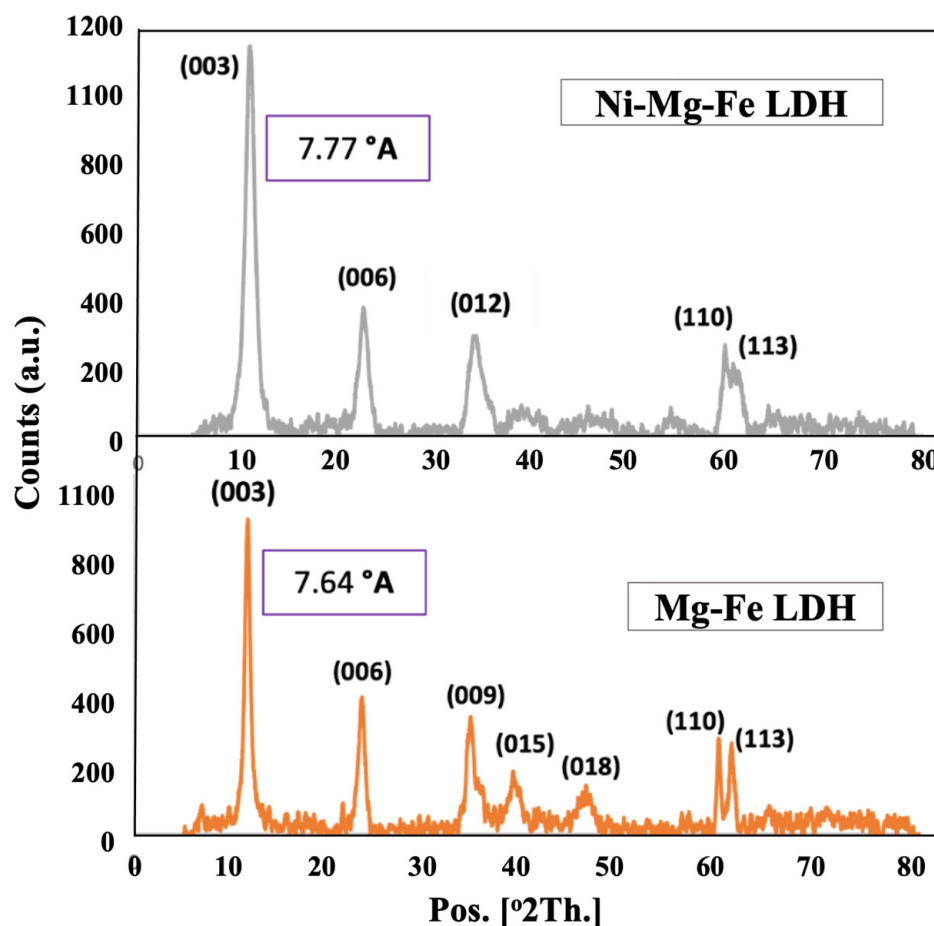


Figure 3. XRD patterns of the Mg-Fe LDH and Ni-Mg-Fe LDH catalysts.

2.4. Fourier Transform Infrared Spectroscopy (FTIR)

Figure 4 shows the FTIR spectra of the Mg-Fe LDH and Ni-Mg-Fe LDH samples, which had similar IR bands. The broad and strong signal at 3400–3450 cm^{-1} is the –O–H stretching band, arising from the interlayer water molecules and the metal-hydroxyl group [62]. The small and weak intensity band centered at approximately 1630–1639 cm^{-1} can be ascribed to the bending vibration of water H–OH–. The band at 1350 cm^{-1} can be assigned to the vibration of the interlayer CO_3^{2-} and NO_3^- anions. The broad peaks at 550 cm^{-1} and 750 cm^{-1} could be assigned to the M–O, O–M–O, and M–O–M (M = Fe, Mg, Ni, Co, and Cu) vibrations [63].

2.5. N_2 Physisorption Measurement

Figure 5 illustrates the nitrogen adsorption–desorption for a series of synthesized catalysts, which were examined to estimate their specific surface area and porosity. According to the IUPAC classification [64], the Mg-Fe LDH showed a type II isotherm, while the Ni-Mg-Fe LDH showed type IV. The Mg-Fe LDH showed H2 type hysteresis loops, indicating nonrigid aggregates of plate-like particles that were solid with a wide pore size distribution, while the Ni-Mg-Fe LDH exhibited the typical H3 type, indicating that the type of holes were slit pores formed by the aggregation of sheet particles [64,65]. The pore

size distribution analysis, using the pore diameter, revealed that all the samples had bimodal distribution curves in the microporous and mesoporous ranges. Table 1 summarizes the textural properties of all investigated catalysts. The BET surface area of the Ni-Mg-Fe LDH was $143 \text{ m}^2/\text{g}$, which is two times larger than that of the Mg-Fe LDH ($70 \text{ m}^2/\text{g}$). The pronounced elevation of the specific surface area could be attributed to the small crystallite size of this particular catalyst.

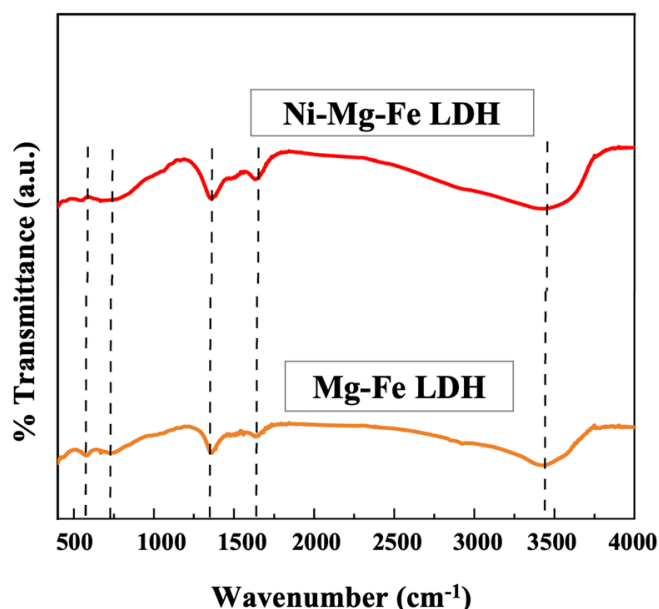


Figure 4. FTIR spectra of the Mg-Fe LDH and Ni-Mg-Fe LDH catalysts.

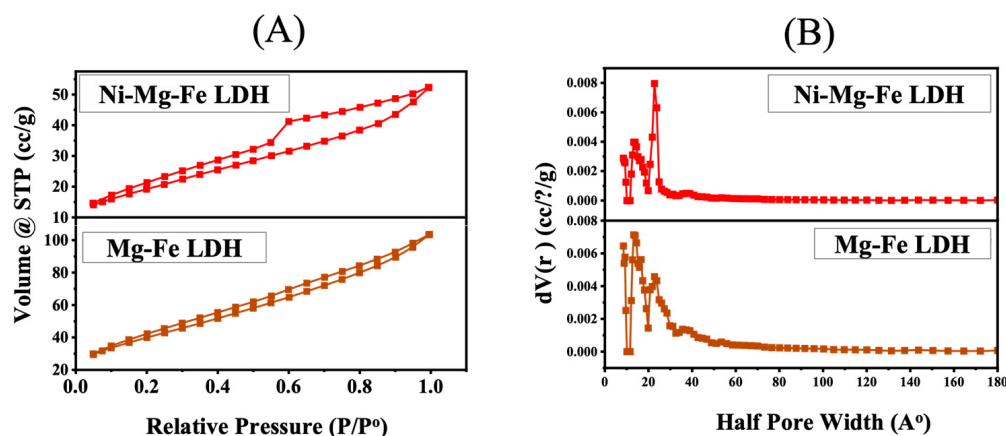


Figure 5. (A) N_2 adsorption–desorption isotherms; (B) pore size distribution curves for the Mg-Fe LDH and Ni-Mg-Fe LDH catalysts.

Table 1. Textural properties of the different catalysts from N_2 - physisorption.

Sample	S_{BET} (m^2/g)	S_{micro} (m^2/g)	S_{meso} (m^2/g)	V_{total} (cc/g)	V_{micro} (cc/g)	V_{meso} (cc/g)	Average Pore Size (nm)
Ni-Mg-Fe LDH	143	35.6	27	0.08	0.03	0.05	2.3
Mg-Fe LDH	70	76.13	57.6	0.16	0.05	0.1	2.2

2.6. Temperature-Programmed Desorption (TPD- CO_2)

The basic properties of the catalysts were assessed using the temperature-programmed desorption of CO_2 . The temperatures at which the chemisorbed peaks appeared can be used to relate the peaks. The peaks that decompose at low and moderate temperatures (between

100 and 420 °C) are where bicarbonate and bidentate species can be found. There were monodentate species present, which is why the peak decomposed at a higher temperature (540 °C) [66]. From the deconvoluted peaks in Figure 6, it is revealed that each catalyst had different types of basic sites. The TPD-CO₂ profiles of all of the hybrid catalysts show peaks within the range of 100–700 °C due to the desorption of weakly bonded CO and the breakdown of carbonate ions that existed in the interlayer of the LDH samples. In the hybrid catalysts' TPD-CO₂ profiles, the peaks extended to approximately 620 °C, leading to tightly bonded monodentate or bidentate carbonate species. In addition, there was a peak at approximately 350 °C, which is attributed to bicarbonate species connected to weak or medium basic strength sites [67]. From Table 2, it is obvious that the Mg-Fe LDH catalyst had a higher total number of basic sites (1096.44 μmol/g).

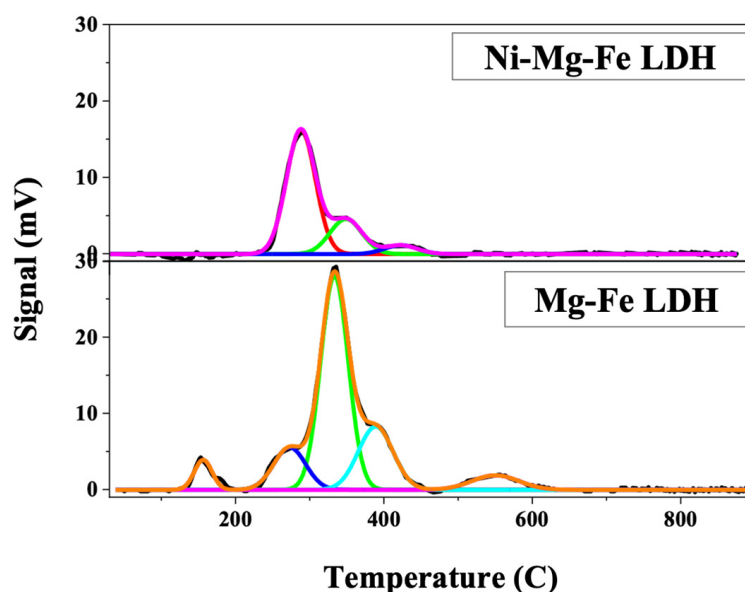


Figure 6. CO₂-TPD patterns of the Mg-Fe LDH and Ni-Mg-Fe LDH catalysts.

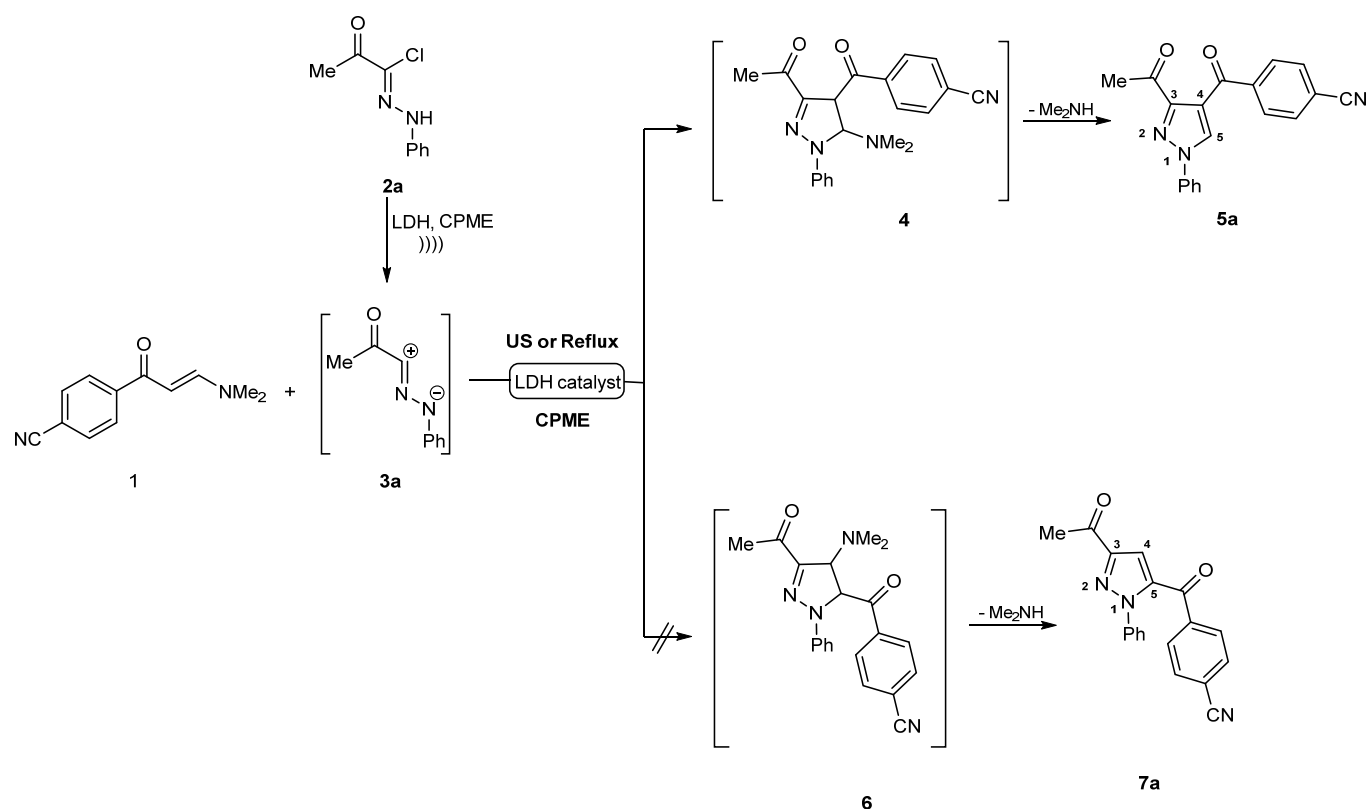
Table 2. Data obtained from the CO₂-TPD profile analyses of all investigated samples.

Catalyst	Temp. (°C)	CO ₂ Uptake (μmol/g)	Total CO ₂ Uptake (μmol/g)
Ni-Mg-Fe LDH	288.1	439.74	626.45
	348.8	143.71	
	422.8	43.01	
Mg-Fe LDH	156.3	59.59	1096.44
	333.3	593.67	
	272.9	142.12	
	388.8	226.34	
	550.2	74.72	

2.7. Catalytic Activity Study

We initiated our study with the reaction of enamionone, named *E*-4-(3-(dimethylamino)acryloyl)benzoxonitrile (**1**), and hydrazonyl chloride (**2a**) (Scheme 1). This reaction, illustrated in Scheme 1, was taken as a model reaction to optimize the reaction conditions (Table 3).

Inspired by our previous work [28], we decided to test two different LDH catalysts: Mg-Fe(III) LDH and Ni-Mg-Fe(III) LDH. Initially, the reaction between equimolar amounts of enamionone (**1**) and hydrazonyl chloride (**2a**) in CPME solvent and the presence of 0.1 g catalyst under ultrasonic conditions (US irradiations) was performed (Table 3).



Scheme 1. Optimization of the reaction conditions for the 1,3-dipolar cycloaddition reaction.

Table 3. Screening of the reaction conditions for the synthesis of pyrazoles.

Entry	Catalyst/wt	Solvent	Temp. (°C)	US Irradiation		Silent Condition	
				Yield (%)	Time (Min.)	Yield (%)	Time
1	none	CPME	80	-	180	-	10 h
2	Mg- Fe (III) LDH [2:1]/0.1 g	CPME	80	90	30	76	4 h
3	Ni- Mg- Fe (III) LDH [1:1:1]/0.1 g	CPME	80	98	15	90	1.5 h
4	Ni- Mg- Fe (III) LDH [1:1:1]/0.15 g	CPME	80	98	15	90	1.5 h
5	Ni- Mg -Fe (III) LDH [1:1:1]/0.1 g	Benzene	80	99	15	93	1.5 h
6	Ni- Mg -Fe (III) LDH [1:1:1]/0.1 g	CHCl ₃	80	81	15	69	2 h
7	Ni- Mg -Fe (III) LDH [1:1:1]/0.1 g	THF	80	89	15	81	2 h

Table 3 shows the excellent yield of the obtained product (98%) attained using the Ni-Mg-Fe(III) LDH as a catalyst at 80 °C under ultrasonic irradiation for 15 min. (Table 3, entry 3). In addition, the product was obtained via the other LDH catalysts in good yield (Table 3, entry 2). Next, the best catalyst was tested at 0.15 g under the same reaction conditions, which did not reveal any superior efficacy (Table 3, entry 4). In addition, under ultrasonic irradiation, no product formed without a catalyst (entry 1). All reactions were performed under silent reaction conditions (without ultrasonic irradiation) (Table 3). However, a lower yield and long reaction times were noted under conventional reaction

conditions, thus proving the significant effect of ultrasound on the synthesis of pyrazole in the present methodology. In addition, the effect of different solvents was tested to address the beneficial impact of CPME in this reaction (Table 3, entries 5–7). It is worth mentioning that CPME was an effective solvent for conducting the 1,3-dipolar cycloaddition reaction over the hazardous benzene, chloroform, or THF. Although the reaction yield in benzene was slightly higher than in CPME, the low vaporization energy of CPME makes it a good choice in ultrasonic reaction media, allowing for easy recycling of the solvent by the usual extractive workup. It is crucial to find a rationale for the enhancement effect of the ultrasound irradiation on the above reaction, since the reaction proceeded under silent conditions, resulting in a longer reaction time and a lower yield (entries 2 and 3). It has been established that heterogeneous catalytic reactions, such as those investigated between solids and liquids, are enhanced by mechanical effects that are caused by violent bubble collapse at the interface. Furthermore, shockwaves can break polar and nonvolatile molecules at the bubble–liquid interface. A competitive, simultaneously polar and radical pathway is considered plausible from this point of view. Ultrasonication usually results in an overall acceleration and a different product distribution when silent and ultrasonic reactions converge to the same product(s) [46], based on the well-established and reported spectroscopic procedure for 2D ^1H - ^{13}C HMBC NMR (*cf.* supporting information) [68]. This reaction proceeded regioselectively between the enaminone and the nitrilimine **3a** (generated in situ), which afforded only one isolable product in each case, as examined by thin layer chromatography (TLC). The isolated product may be formulated as **5a** or **7a** (Scheme 1). Therefore, the formed product was identified as **5a**, and structure **7a** was ruled out (Scheme 1). Figure 7 shows the diagnostic correlation between the pyrazole proton and carbons in each case, although for both suggested structures, **5a** or **7a**, a four correlation for the pyrazole proton appeared with carbons, the regioisomer **5a** showed a correlation with one carbonyl function group. On this basis, we ruled out the other regioisomer **7a**.

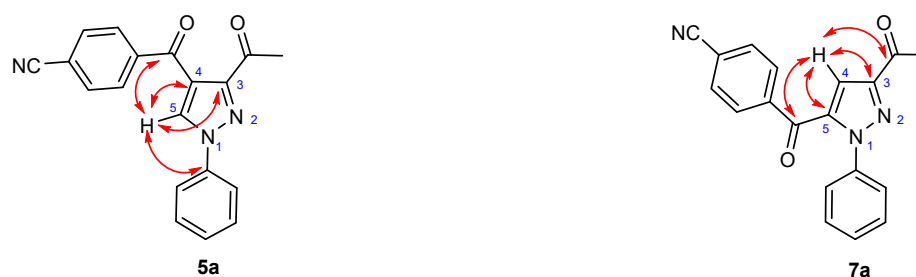


Figure 7. Diagnostic correlations in the ^1H - ^{13}C HMBC (red arrows) for the two regioisomers **5a** and **7a**.

The scope and generality of the present methodology were tested by synthesizing different pyrazole derivatives using the Ni-Mg-Fe (III) LDH (0.1 g) catalyst under the optimized reaction conditions (Scheme 2).

Products **5a–d** were obtained with good yields (90–98%) (Figure 8).

Compounds **5a–d** were in complete agreement with the analytical and spectroscopic data.

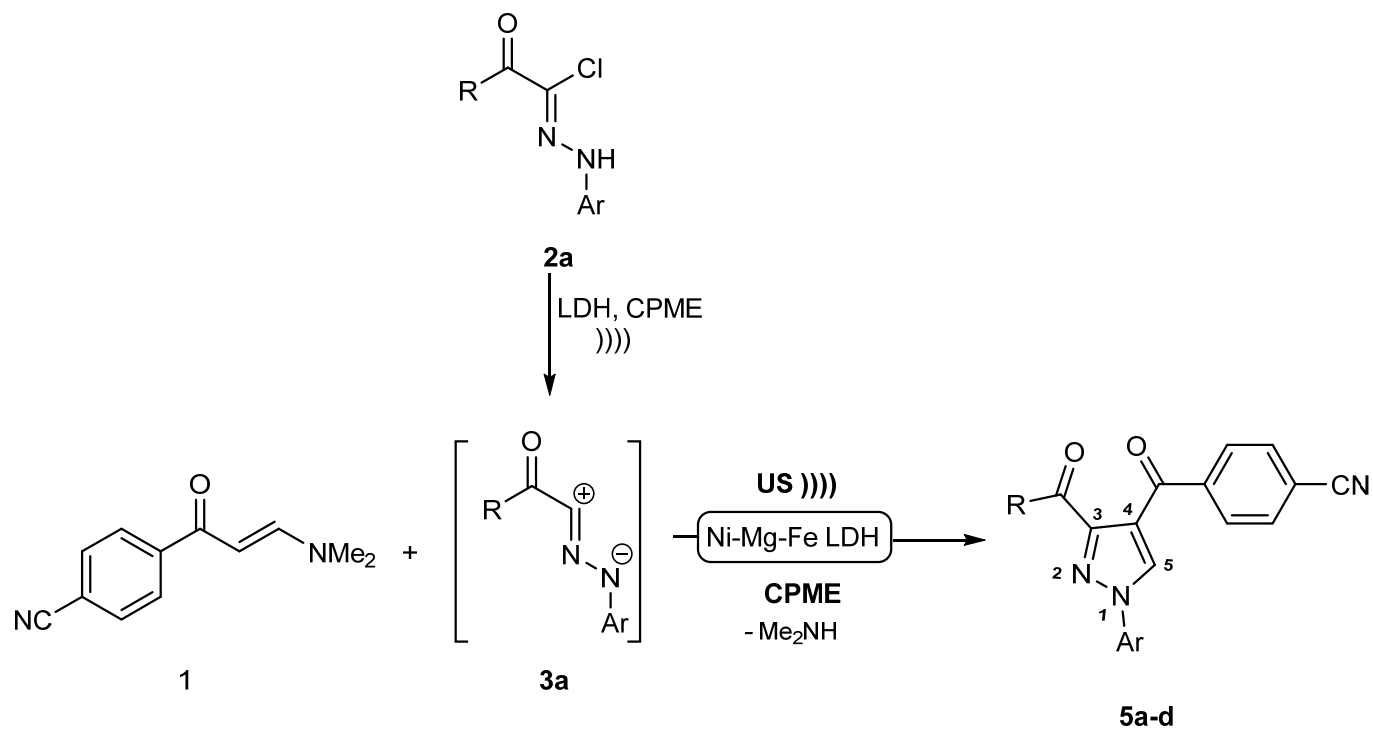
The superiority of the Ni-Mg-Fe LDH over the other LDH used is accredited to the small crystallite size, large surface area, and mesoporosity, which assist a greater number of reactant molecules in reacting efficiently on the basic centers of the Ni-Mg-Fe LDH catalyst.

The recyclability of the prepared catalyst, Ni-Mg-Fe(III) LDH, was also studied via filtration each time and reused after drying for the model reaction. It was observed that the catalyst could be reused up to six consecutive catalytic cycles without any significant loss in activity (Figure 9).

The slight decay in yield is due to the catalyst's weight loss during the workup of the successive runs.

A tentative mechanism was proposed for the above reaction in which the creation of novel pyrazole derivatives **5a–d** were supposed to be formed via initial 1,3-dipolar cycloaddition of the nitrilimines **3a–d** (liberated in situ by the action of the large surface area, porosity, and basicity of the Ni-Mg-Fe LDH catalyst, causing dehydrohalogenation

(−HCl) (Scheme 1) to the stimulated double bond in the enaminone 1 to pay for the non-isolable dihydro pyrazole transition state liaises 4, tracked by the elimination of dimethylamine (improved by the reaction with the inattentive HCl), yielding the pyrazole derivative 5a–d.



Scheme 2. The scope of green access for the synthesis of the novel pyrazoles.

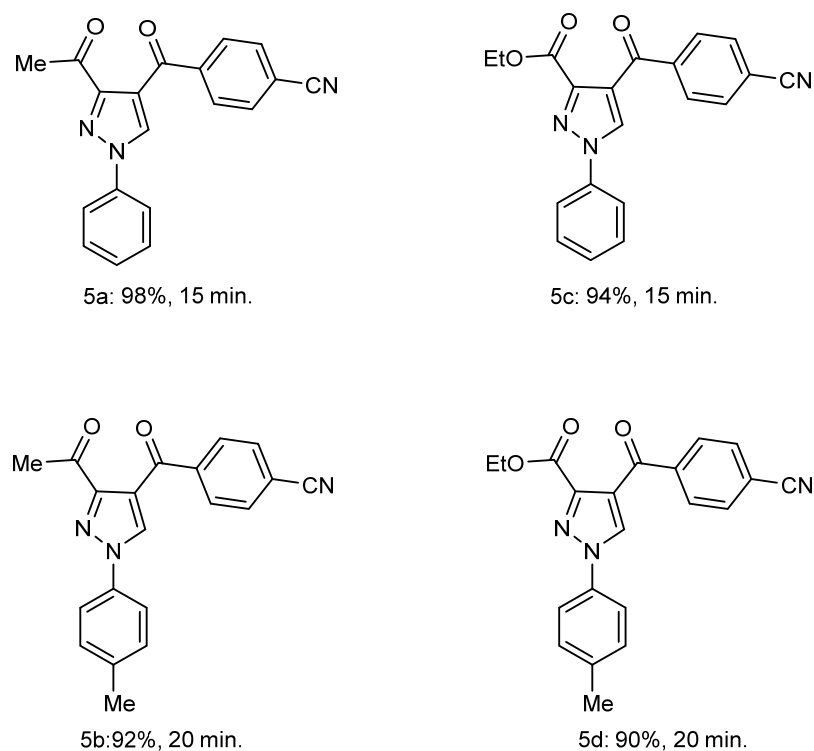


Figure 8. Scope of the synthesis of the pyrazole derivatives.

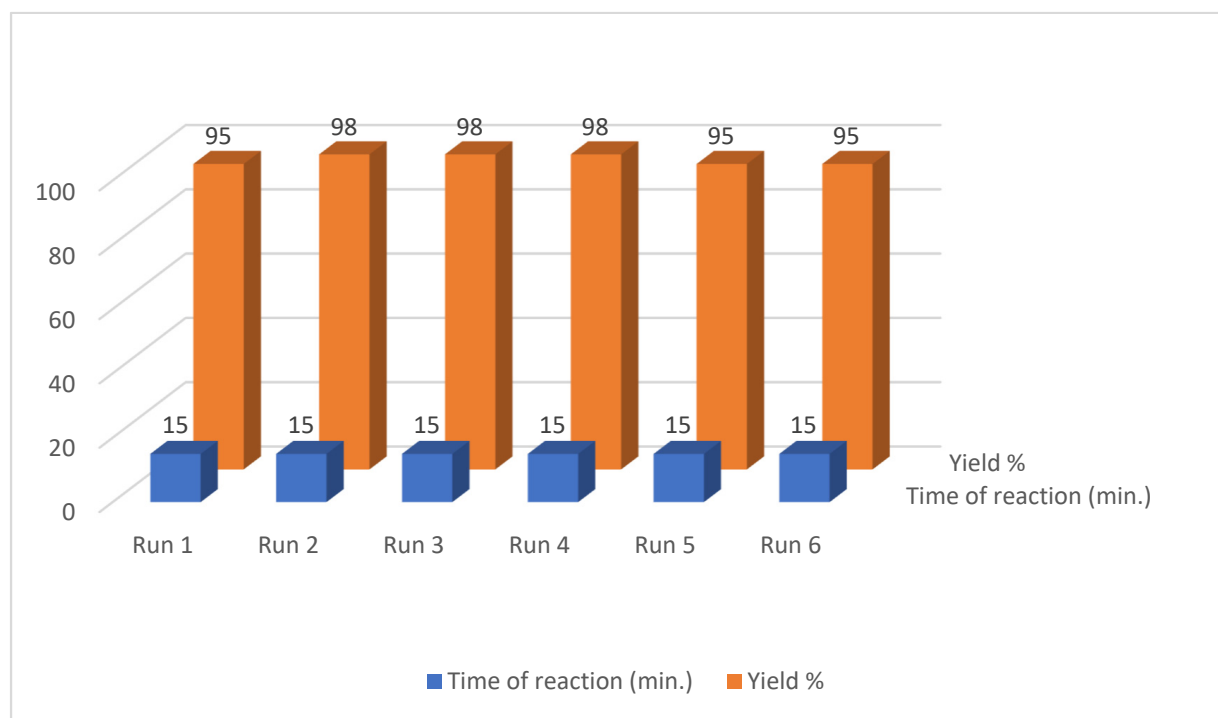


Figure 9. Reusability of the Ni-Mg-Fe LDH catalyst for synthesis of 5a.

3. Conclusions

We report an efficient ultrasound-assisted sustainable protocol for the regioselective synthesis of novel pyrazoles via 1,3-dipolar cycloaddition reaction over different LDH base solid catalysts. The Ni-Mg-Fe LDH catalyst showed a significant advantage over all the investigated LDH-based catalysts. The controlling factors of LDH on this reaction were based on the surface area, porosity, and basicity of the used LDH catalyst. The ultrasound irradiation method offered high yields of pyrazole derivatives in a short reaction time over the Ni-Mg-Fe LDH solid catalyst. The recyclability experiment advises the excellent reusability of this Ni-Mg-Fe LDH catalyst. Introducing CPME into the 1,3-dipolar cycloaddition reaction opens new horizons for such reactions in a safe and environmentally friendly solvent, avoiding the dangerous effects of nonpolar volatile solvents and the limitations of solvent-free reactions.

4. Experimental

4.1. General

4.1.1. Materials for Catalyst Synthesis

The chemical reagents used for the catalysts' synthesis included ferric nitrate nonahydrate and nickel(II)nitrate hexahydrate from Fluka, Buchs, Switzerland; magnesium nitrate hexahydrate from Koch-Light, Haverhill, UK; sodium carbonate and sodium hydroxide from Sigma-Aldrich Laborchemikalien GmbH; distilled/deionized water; N₂ gas cylinders, Abdullah Hashim Ltd., Jeddah, Saudi Arabia.

4.1.2. Catalyst Characterization Techniques

Thermogravimetric Analysis (TGA)

TGA is used to characterize materials for their thermal stability and their quantity of layered double hydroxide water by monitoring weight loss or phase changes from the material to the temperature [69]. Thermogravimetry (TG) and differential scanning calorimetric (DSC) analyses of the different solid samples were performed on a Netzsch system STA 449 F3 Jupiter–Simultaneous Thermal Analyzer. The TGA DSC was operated in an air flow at a heating rate of 25 °C/min up to 800 °C. In each run, 6–10 mg was placed

in the platinum pan under a flow of nitrogen atmosphere of 40 mL min⁻¹ and at a heating rate of 10 °C min⁻¹.

X-ray Diffraction (XRD)

X-ray diffraction (XRD) is one of the primary techniques used by mineralogists and solid-state chemists for the characterization of crystalline solids and determination of their structure [70]. X-ray diffraction (XRD) studies were performed for all prepared solid samples using a Bruker diffractometer (Bruker D8 advance target). The patterns were run with Cu K α and a monochromator ($\lambda = 1.5405 \text{ \AA}$) at 40 kV and 40 mA. The crystallite size phases were calculated using the Scherer equation: $d \text{ (nm)} = B\lambda / \beta \frac{1}{2} \cos \theta$, where d is the average crystallite size of the phase under investigation; B is the Scherer constant (0.89); λ is the wavelength of the X-ray beam used (1.5405 Å); $\beta \frac{1}{2}$ is the full width at half maximum (FWHM) of the diffraction peak; and θ is the diffraction angle.

Fourier Transform Infrared Spectroscopy (FTIR)

FT-IR spectroscopy is often used to classify structures because functional groups generate characteristic bands in terms of both the intensity and location (i.e., frequency). The position of a large number of characteristic bands are known and tabulated in the FTIR library [71]. Fourier transform infrared (FTIR) spectroscopy of the samples was performed using a PerkinElmer UATR Two FT-IR spectrometer. The measurements were carried out in the wavenumber range 4000–400 cm⁻¹ after 32 scans.

Temperature-Programmed Desorption (TPD-CO₂)

Temperature-programmed desorption (TPD) is an analysis technique allowing for programmed temperature changes revealing the strength and number of active sites under a range of reaction conditions [72]. Temperature-programmed desorption was first described by Amenomiya and Cvetanovic in 1963 [73]. In TPD studies, a solid specimen previously equilibrated with adsorbate under well-defined conditions, immediately prior to the analysis, is submitted to programmed temperature elevation. TPD-CO₂ was performed in an atmospheric pressure microreactor connected to a TCD via a heated quartz capillary. The catalyst ($\approx 60 \text{ mg}$) was heated at 100 °C in flowing helium for 1 hr in order to remove the physically adsorbed water. The sample was then cooled to 30 °C and exposed to CO₂ (10% CO₂ in nitrogen) for 1 h. After this, the system was purged in flowing helium for 30 min to remove any physisorbed CO₂ and then the temperature was increased from 30 °C to 800 °C at a rate of 10 °C min⁻¹ under a flow of helium gas at a flow rate of 90 mL min⁻¹. The concentration of the CO₂ desorbed into the helium carrier gas was monitored with the TCD. Prior to each TPD experiment, the response of the TCD was calibrated by the calibration curve of the peak area and injected gas volume. The TPD-CO₂ experiments were evaluated using OriginPro Software.

Nitrogen Adsorption/Desorption (N₂ Physisorption)

Adsorption is an increase in the density of the fluid in the area of the interface, occurring when a solid surface is exposed to a gas or liquid [74]. Gas adsorption is of major importance for the characterization of a wide range of porous materials. Of all the many gases and vapors that are readily available and can be used as adsorptives, nitrogen has remained universally pre-eminent. With the aid of user-friendly commercial equipment and online data processing, it is now possible to use nitrogen adsorption at 77 K for both routine quality control and the investigation of new materials [75]. The adsorption techniques presented in this work is physisorption. Physisorption occurs as a gas molecule approaches the surface of the solid where it experiences London dispersion forces of attraction, as well as short-range repulsion forces. At a particular distance from the surface, these forces balance each other to minimize the potential energy, and the gas molecule is physisorbed [76]. The texture properties of the prepared samples were determined from nitrogen adsorption/desorption isotherms measured at 77 K using a model NOVA

3200e automated gas sorption system (Quantachrome, USA). Prior to the measurement, a sample was degassed for 3 h at 100 °C. The surface area, SBET, was calculated by applying the Brunauer-Emmett-Teller (BET) equation [77]. The average pore radius was estimated from the relation $2V_p/S_{BET}$, where V_p is the total pore volume (at $P/P^0 = 0.975$). The pore size distribution over a mesopore range was generated by a Barrett-Joyner-Halenda (BJH) analysis of the desorption branches, and the values for the average pore sizes were calculated [78].

4.1.3. Catalytic Organic Reaction

All organic solvents were purchased from commercial sources and used as received unless otherwise stated. All other chemicals were purchased from Merck, Aldrich, Laborchemikalien GmbH or Acros, Belgium and used without further purification. Thin layer chromatography (TLC) was performed on precoated Merck 60 GF254 silica gel plates, Laborchemikalien GmbH with a fluorescent indicator and detection by means of UV light at 254 and 360 nm. The melting points were measured on a Stuart melting point apparatus and are uncorrected. The IR spectra were recorded on a Smart iTR, which is an ultrahigh-performance, versatile attenuated total reflectance (ATR) sampling accessory on the Nicolet iS10 FT-IR spectrometer. The NMR spectra were recorded on a Bruker Avance III 400 (9.4 T, 400.13 MHz for ^1H , 100.62 MHz for ^{13}C analysis) spectrometer, Switzerland with a 5 mm BBFO probe at 298 K. Chemical shifts (δ in ppm) are given relative to internal solvent, DMSO. The mass spectra for the synthesized derivatives were recorded using a Thermo ISQ Single Quadrupole GC-MS instrument, USA. An elemental analysis was carried out using a Euro Vector EA3000 Series C, H, N, and S analyzer, Italy. The sonication was performed using the Elma Sonicator P30H instrument, Germany with an ultrasound frequency of 37 kHz and power of 320 W (max.). The bath temperature was raised from 25 °C to 80 °C after 30 min of operation. All reactions were carried out at 80 °C, which was maintained by adding or removing the water in an ultrasonic bath (the temperature inside the reaction vessel was 76–79 °C).

According to the reported literature, enaminone **1** [79] and α -ketohydrazoneyl halides **2a–d** [80] were prepared.

4.2. General Procedures for the Synthesized Pyrazoles **5a–d** Derivatives

4.2.1. Method A (under Ultrasonic Irradiations (US))

To a mixture of enaminone **1** (10 mmol) and the appropriate hydrazoneyl chloride **3a–d** (10 mmol) in CPME (25 mL), an 0.1 g of LDH was added. The total mixture was placed in a 100 mL round-bottom flask in the sonicator and was irradiated. The reaction flask was exposed to ultrasound irradiations until the reaction was complete. The progress of the reaction was monitored by TLC (eluent; ethyl acetate: chloroform). Upon completion of the reaction, the catalyst was removed by filtration and washed several times with hot ethyl acetate. The filtrate was evaporated under reduced pressure. The obtained solid product was crystallized using ethanol to afford the corresponding pyrazole derivatives **5a–d**.

4.2.2. Method B (Silent Reaction—Without Ultrasonic Irradiation)

The reactions were performed on the same scale described above. The reaction mixture was heated under reflux at 80 °C for the required time to complete the reaction, as monitored by TLC. After the completion of the reaction, the catalyst was removed by filtration, and the products were obtained and purified as described in the previous method.

4.2.3. 4-(3-Acetyl-1-phenyl-1H-pyrazole-4-carbonyl)benzotrile (**5a**)

mp 179–181 °C; IR (KBr) ν/cm^{-1} : 2204 (C \equiv N), 1705, 1674 (C=O), 1601 (C=N); ^1H NMR (DMSO- d_6): δ 2.58 (s, 3H, CH₃), 7.47 (t, 1H, ArH, $J = 7.78$ Hz), 7.62 (t, 2H, ArH, $J = 7.78$ Hz), 7.88 (d, 2H, ArH, $J = 8.15$ Hz), 8.01–8.03 (m, 4H, ArH), 9.12 (s, 1H, pyrazole-H); ^{13}C NMR (DMSO- d_6): δ 27.50, 120.02, 122.61, 124.22, 126.16, 128.60, 130.25, 130.36,

132.62, 132.91, 138.96, 141.03, 150.42, 189.23, 193.32; MS (*m/z*): 315 (M^+). (Found: C, 72.95; H, 4.09; N, 13.21; $C_{19}H_{13}N_3O_2$ requires C, 72.73; H, 4.16; N, 13.33).

4.2.4. 4-(3-Acetyl-1-(*p*-tolyl)-1*H*-pyrazole-4-carbonyl)benzotrile (5b)

mp 187–189 °C; IR (KBr) ν / cm^{-1} : 2206 ($C\equiv N$), 1703, 1673 ($C=O$), 1601 ($C=N$); 1H NMR (DMSO-*d*₆): δ 2.37 (s, 3H, CH_3), 2.56 (s, 3H, CH_3), 7.41 (d, 2H, ArH, $J = 8.3$ Hz), 7.86–7.88 (m, 4H, ArH), 8.03 (d, 2H, ArH, $J = 8.3$ Hz), 9.04 (s, 1H, pyrazole-H); ^{13}C NMR (DMSO-*d*₆): δ 20.95, 27.45, 119.95, 122.48, 124.22, 126.12, 130.22, 130.65, 132.25, 133.06, 136.72, 138.36, 141.02, 150.27, 189.38, 193.53; MS (*m/z*): 329 (M^+). (Found: C, 73.13; H, 4.54; N, 12.66; $C_{20}H_{15}N_3O_2$ requires C, 72.94; H, 4.59; N, 12.76).

4.2.5. Ethyl 4-(4-Cyanobenzoyl)-1-phenyl-1*H*-pyrazole-3-carboxylate (5c)

mp 121–123 °C; IR (KBr) ν / cm^{-1} : 2204 ($C\equiv N$), 1710, 1668 ($C=O$), 1596 ($C=N$); 1H NMR (DMSO-*d*₆): δ 1.00 (t, 3H, CH_3 , $J = 7.4$ Hz), 4.11 (q, 2H, CH_2 , $J = 7.4$ Hz), 7.45 (t, 1H, ArH, $J = 7.6$ Hz), 7.57 (t, 2H, ArH, $J = 8.4$ Hz), 7.95 (d, 2H, ArH, $J = 8.4$ Hz), 7.97 (d, 2H, ArH, $J = 8.4$ Hz), 8.05 (d, 2H, ArH, $J = 8.2$), 9.15 (s, 1H, pyrazole-H); ^{13}C NMR (DMSO-*d*₆): δ 13.96, 61.62, 120.10, 123.38, 124.24, 126.25, 128.69, 130.23, 130.34, 132.86, 133.04, 138.93, 141.35, 144.17, 161.51, 188.19; MS (*m/z*): 345 (M^+). (Found: C, 69.75; H, 4.29; N, 12.06; $C_{20}H_{15}N_3O_3$ requires C, 69.56; H, 4.34; N, 12.17).

4.2.6. Ethyl 4-(4-Cyanobenzoyl)-1-(*p*-tolyl)-1*H*-pyrazole-3-carboxylate (5d)

mp 133–135 °C; IR (KBr) ν / cm^{-1} : 2204 ($C\equiv N$), 1707, 1661 ($C=O$), 1602 ($C=N$); 1H NMR (DMSO-*d*₆): δ 1.01 (t, 3H, CH_3 , $J = 7.2$ Hz), 2.41 (s, 3H, CH_3), 4.23 (q, 2H, CH_2 , $J = 7.4$ Hz), 7.43 (d, 2H, ArH, $J = 8.4$ Hz), 7.93–7.95 (m, 4H, ArH), 8.06 (d, 2H, ArH, $J = 8.4$ Hz), 9.08 (s, 1H, pyrazole-H); ^{13}C NMR (DMSO-*d*₆): δ 13.79, 20.83, 61.51, 120.10, 123.46, 124.26, 126.25, 130.21, 131.44, 132.32, 133.74, 137.11, 138.15, 141.65, 145.23, 160.49, 187.56; MS (*m/z*): 359 (M^+). (Found: C, 70.39; H, 4.71; N, 11.56; $C_{21}H_{17}N_3O_3$ requires C, 70.18; H, 4.77; N, 11.69).

Supplementary Materials: The following supporting information can be downloaded at: <https://www.mdpi.com/article/10.3390/catal13040650/s1>, Figure S1: 1H NMR of compound 5a, Figure S2: ^{13}C NMR of compound 5a, Figure S3: 1H NMR of compound 5b, Figure S4: ^{13}C NMR of compound 5b, Figure S5: 1H NMR of compound 5c, Figure S6: ^{13}C NMR of compound 5c, Figure S7: 1H - ^{13}C -HMBC NMR that show one correlation between the pyrazole proton towards one carbonyl only.

Author Contributions: Conceptualization, M.A.S. and A.N.A.-R., methodology, E.S.I., M.A.S., A.N.A.-R. and T.S.S.; Original draft preparation, T.S.S., E.S.I. and M.M.M.M.; Writing—review and editing, all the authors, M.M.M.M. and A.N.A.-R.; Supervision, M.M.M.M., and A.N.A.-R. All authors have read and agreed to the published version of the manuscript.

Funding: This project was funded by the Deanship of Scientific Research (DSR) at King Abdulaziz University, Jeddah, under grant no. (G:822–130–1441).

Data Availability Statement: Data available on request.

Acknowledgments: This project was funded by the Deanship of Scientific Research (DSR) at King Abdulaziz University, Jeddah, under grant no. (G:822–130–1441). The authors, therefore, acknowledge with thanks the DSR for the technical and financial support.

Conflicts of Interest: The authors declare no conflict of interest.

References

1. Fustero, S.; Sanchez-Rosello, M.; Barrio, P.; Simon-Fuentes, A. From 2000 to mid-2010: A fruitful decade for the synthesis of pyrazoles. *Chem. Rev.* **2011**, *111*, 6984–7034. [[CrossRef](#)] [[PubMed](#)]
2. Liu, X.-H.; Cui, P.; Song, B.-A.; Bhadury, P.S.; Zhu, H.-L.; Wang, S.F. Synthesis, structure and antibacterial activity of novel 1-(5-substituted-3-substituted-4, 5-dihydropyrazol-1-yl) ethanone oxime ester derivatives. *Bioorganic Med. Chem.* **2008**, *16*, 4075–4082. [[CrossRef](#)] [[PubMed](#)]

3. Foks, H.; Pancechowska-Ksepko, D.; Kędzia, A.; Zwolska, Z.; Janowiec, M.; Augustynowicz-Kopeć, E. Synthesis and antibacterial activity of 1H-pyrazolo [3, 4-b] pyrazine and-pyridine derivatives. *Farmaco* **2005**, *60*, 513–517. [[CrossRef](#)]
4. Gilbert, A.M.; Failli, A.; Shumsky, J.; Yang, Y.; Severin, A.; Singh, G.; Hu, W.; Keeney, D.; Petersen, P.J.; Katz, A.H. Pyrazolidine-3, 5-diones and 5-hydroxy-1 H-pyrazol-3 (2 H)-ones, inhibitors of UDP-N-acetylenolpyruvyl glucosamine reductase. *J. Med. Chem.* **2006**, *49*, 6027–6036. [[CrossRef](#)]
5. Shamroukh, A.; Zaki, M.; Morsy, E.; Abdel-Motti, F.; Abdel-Megeid, F. Preparation and identification of some new pyrazolo pyrin derivatives. *Arch. Pharm. Chem. Life Sci.* **2007**, *14*, 340–345.
6. Prakash, O.; Kumar, R.; Parkash, V. Synthesis and antifungal activity of some new 3-hydroxy-2-(1-phenyl-3-aryl-4-pyrazolyl) chromones. *Eur. J. Med. Chem.* **2008**, *43*, 435–440. [[CrossRef](#)] [[PubMed](#)]
7. Storer, R.; Ashton, C.J.; Baxter, A.D.; Hann, M.M.; Marr, C.L.; Mason, A.M.; Mo, C.-L.; Myers, P.L.; Noble, S.A.; Penn, C.R. The synthesis and antiviral activity of 4-fluoro-1-β-D-ribofuranosyl-1H-pyrazole-3-carboxamide. *Nucleosides Nucleotides Nucleic Acids* **1999**, *18*, 203–216. [[CrossRef](#)]
8. Genin, M.J.; Biles, C.; Keiser, B.J.; Poppe, S.M.; Swaney, S.M.; Tarpley, W.G.; Yagi, Y.; Romero, D.L. Novel 1, 5-diphenylpyrazole nonnucleoside HIV-1 reverse transcriptase inhibitors with enhanced activity versus the delavirdine-resistant P236L mutant: Lead identification and SAR of 3-and 4-substituted derivatives. *J. Med. Chem.* **2000**, *43*, 1034–1040. [[CrossRef](#)]
9. Daidone, G.; Maggio, B.; Plescia, S.; Raffa, D.; Musiu, C.; Milia, C.; Perra, G.; Marongiu, M.E. Antimicrobial and antineoplastic activities of new 4-diazopyrazole derivatives. *Eur. J. Med. Chem.* **1998**, *33*, 375–382. [[CrossRef](#)]
10. Gamage, S.A.; Spicer, J.A.; Rewcastle, G.W.; Milton, J.; Sohal, S.; Dangerfield, W.; Mistry, P.; Vicker, N.; Charlton, P.A.; Denny, W.A. Structure—Activity relationships for pyrido-, imidazo-, pyrazolo-, pyrazino-, and pyrrolophenazinecarboxamides as topoisomerase-targeted anticancer agents. *Eur. J. Med. Chem.* **2002**, *45*, 740–743. [[CrossRef](#)]
11. Comber, R.N.; Gray, R.J.; Secrist, J.A., III. Acyclic analogues of pyrazofurin: Syntheses and antiviral evaluation. *Carbohydr. Res.* **1992**, *216*, 441–452. [[CrossRef](#)] [[PubMed](#)]
12. Ebenezer, O.; Shapi, M.; Tuszyński, J.A. A Review of the Recent Development in the Synthesis and Biological Evaluations of Pyrazole Derivatives. *Biomedicines* **2022**, *10*, 1124. [[CrossRef](#)] [[PubMed](#)]
13. El-Sehemi, A.G.; Bondock, S.; Ammar, Y.A. Transformations of naproxen into pyrazolecarboxamides: Search for potent anti-inflammatory, analgesic and ulcerogenic agents. *Med. Chem. Res.* **2014**, *23*, 827–838. [[CrossRef](#)]
14. Kadam, P.; Karpoornath, R.; Omondi, B.; Chenia, H.; Ramjugernath, D.; Koorbanally, N.A. Stereo-selective synthesis, structural and antibacterial studies of novel glycosylated b2,3-amino acid analogues. *Med. Chem. Res.* **2015**, *24*, 3174–3193. [[CrossRef](#)]
15. Aggarwal, R.; Bansal, A.; Rozas, I.; Diez-Cecilia, E. P-Toluenesulfonic acid-catalyzed solventfree synthesis and biological evaluation of new 1-(40,60-dimethylpyrimidin-20-yl)-5-amino-4H-3-arylpyrazole derivatives. *Med. Chem. Res.* **2014**, *23*, 1454–1464. [[CrossRef](#)]
16. Sawant, S.D.; Lakshma Reddy, G.; Dar, M.I.; Srinivas, M.; Gupta, G.; Sahu, P.K.; Mahajan, P.; Nargotra, A.; Singh, S.; Sharma, S.C.; et al. Discovery of novel pyrazolopyrimidinone analogs as potent inhibitors of phosphodiesterase type-5. *Bioorg. Med. Chem.* **2015**, *23*, 2121–2128. [[CrossRef](#)] [[PubMed](#)]
17. Küçükgülzel, S.G.; Senkardes, S. Recent advances in bioactive pyrazoles. *Eur. J. Med. Chem.* **2015**, *97*, 786–815. [[CrossRef](#)]
18. Tseng, S.L.; Hung, M.S.; Chang, C.P.; Song, J.S.; Tai, C.L.; Chiu, H.H.; Hsieh, W.P.; Lin, Y.; Chung, W.L.; Kuo, C.; et al. Bioisosteric replacement of the pyrazole 5-sryl moiety of N-(piperidin-1-yl)-5-(4-chlorophenyl)-1-(2,4-dichlorophenyl)-4-methyl-1H-pyrazole-3-carboxamide (SR141716A). A novel series of alkynylthiophenes as potent and selective cannabinoid-1 receptor antagonists. *J. Med. Chem.* **2008**, *51*, 5397–5412.
19. Guo, Y.H.; Wang, G.D.; Wei, L.; Wan, J.P. Domino C-H Sulfonylation and Pyrazole Annulation for Fully Substituted Pyrazole Synthesis in Water Using Hydrophilic Enaminones. *J. Org. Chem.* **2019**, *84*, 2984–2990. [[CrossRef](#)]
20. Xu, Y.H.; Chen, Q.L.; Tian, Y.S.; Wu, W.; You, Y.; Weng, Z.Q. Silver-catalyzed synthesis of 5-aryl-3-trifluoromethyl pyrazoles. *Tetrahedron Lett.* **2020**, *61*, 151455. [[CrossRef](#)]
21. Golovanov, A.A.; Odin, I.S.; Gusev, D.M.; Vologzhanina, A.V.; Sosnin, I.M.; Grabovskiy, S.A. Reactivity of Cross-Conjugated Enynones in Cyclocondensations with Hydrazines: Synthesis of Pyrazoles and Pyrazolines. *J. Org. Chem.* **2021**, *86*, 7229–7241. [[CrossRef](#)]
22. Fang, Z.; Yin, H.; Lin, L.; Wen, S.; Xie, L.; Huang, Y.; Weng, Z. Collaborative Activation of Trifluoroacetyl Diazoester by a Lewis Acid and Base for the Synthesis of Polysubstituted 4-Trifluoromethylpyrazoles. *J. Org. Chem.* **2020**, *85*, 8714–8722. [[CrossRef](#)] [[PubMed](#)]
23. Veerakanellore, G.B.; Smith, C.M.; Vasiliu, M.; Oliver, A.G.; Dixon, D.A.; Carrick, J.D. Synthesis of 1H-Pyrazol-5-yl-pyridin-2-yl-1,2,4 triazinyl Soft-Lewis Basic Complexants via Metal and Oxidant Free 3+2 Dipolar Cycloaddition of Terminal Ethynyl Pyridines with Tosylhydrazides. *J. Org. Chem.* **2019**, *84*, 14558–14570. [[CrossRef](#)] [[PubMed](#)]
24. Abd Al-Mohson, Z.M. Synthesis of novel pyrazole derivatives containing tetrahydrocarbazole, antimicrobail evaluation and molecular properties. *Eurasian Chem. Commun.* **2021**, *3*, 421–434.
25. Salih, A.; Al-Messri, Z.A.K. Synthesis of pyranopyrazole and pyranopyrimidine derivatives using magnesium oxide nanoparticles and evaluation as corrosion inhibitors for lubricants. *Eurasian Chem. Commun.* **2021**, *3*, 533–541.
26. Farag, A.M.; Mayhoub, A.S.; Barakat, S.E.; Bayomi, A.H. Regioselective synthesis and antitumor screening of some novel N-phenylpyrazole derivatives. *Bioorganic Med. Chem.* **2008**, *16*, 881–889. [[CrossRef](#)] [[PubMed](#)]

27. Donohue, S.R.; Halldin, C.; Pike, V.W. A facile and regioselective synthesis of rimonabant through an enamine-directed 1, 3-dipolar cycloaddition. *Tetrahedron Lett.* **2008**, *49*, 2789–2791. [[CrossRef](#)]
28. Saleh, T.S.; Narasimharao, K.; Ahmed, N.S.; Basahel, S.N.; Al-Thabaiti, S.A.; Mokhtar, M.J. Mg–Al hydrotalcite as an efficient catalyst for microwave assisted regioselective 1, 3-dipolar cycloaddition of nitrilimines with the enamionone derivatives: A green protocol. *J. Mol. Catal. A Chem.* **2013**, *367*, 12–22. [[CrossRef](#)]
29. Cavani, F.; Trifiro, F.; Vaccari, A. Hydrotalcite-type anionic clays: Preparation, properties and applications. *Catal. Today* **1991**, *11*, 173–301. [[CrossRef](#)]
30. Miyata, S. Anion-exchange properties of hydrotalcite-like compounds. *Clays Clay Miner.* **1983**, *31*, 305–311. [[CrossRef](#)]
31. Yamaoka, T.; Abe, M.; Tsuji, M. Synthesis of Cu Al hydrotalcite like compound and its ion exchange property. *Mater. Res. Bull.* **1989**, *24*, 1183–1199. [[CrossRef](#)]
32. Kirm, I.; Medina, F.; Rodríguez, X.; Cesteros, Y.; Salagre, P.; Sueiras, J. Epoxidation of styrene with hydrogen peroxide using hydrotalcites as heterogeneous catalysts. *Appl. Catal. A Gen.* **2004**, *272*, 175–185. [[CrossRef](#)]
33. Erickson, K.L.; Bostrom, T.E.; Frost, R.L. A study of structural memory effects in synthetic hydrotalcites using environmental SEM. *Mater. Lett.* **2005**, *59*, 226–229. [[CrossRef](#)]
34. Choudary, B.M.; Kantam, M.L.; Reddy, C.R.V.; Rao, K.K.; Figueras, F. The first example of Michael addition catalysed by modified Mg–Al hydrotalcite. *J. Mol. Catal. A Chem.* **1999**, *146*, 279–284. [[CrossRef](#)]
35. Leofanti, G.; Padovan, M.; Tozzola, G.; Venturelli, B. Surface area and pore texture of catalysts. *Catal. Today* **1998**, *41*, 207–219. [[CrossRef](#)]
36. Wang, J.; Ma, J.; Li, X.; Li, Y.; Zhang, G.; Zhang, F.; Fan, X. Cu₂O mesoporous spheres with a high internal diffusion capacity and improved catalytic ability for the aza-Henry reaction driven by visible light. *Chem. Commun.* **2014**, *50*, 14237–14240. [[CrossRef](#)] [[PubMed](#)]
37. Ng, E.-P.; Awala, H.; Ghoy, J.-P.; Vicente, A.; Ling, T.C.; Ng, Y.H.; Mintova, S.; Adam, F. Effects of ultrasonic irradiation on crystallization and structural properties of EMT-type zeolite nanocrystals. *Mater. Chem. Phys.* **2015**, *159*, 38–45. [[CrossRef](#)]
38. Cheong, Y.-W.; Wong, K.-L.; Ling, T.C.; Ng, E.-P. Rapid synthesis of nanocrystalline zeolite W with hierarchical mesoporosity as an efficient solid basic catalyst for nitroaldol Henry reaction of vanillin with nitroethane. *Mater. Express* **2018**, *8*, 463–468. [[CrossRef](#)]
39. Wang, Z.; Huang, L.; Reina, T.R.; Efstathiou, A.M.; Wang, Q. Aqueous Miscible Organic LDH Derived Ni-Based Catalysts for Efficient CO₂ Methanation. *Catalysts* **2020**, *10*, 1168. [[CrossRef](#)]
40. Nope, E.; Sathicq, Á.G.; Martínez, J.J.; Rojas, H.A.; Luque, R.; Romanelli, G.P. Ternary Hydrotalcites in the Multicomponent Synthesis of 4H-Pyrans. *Catalysts* **2020**, *10*, 70. [[CrossRef](#)]
41. Nope, E.; Sathicq, G.; Martínez, J.; Rojas, H.; Luque, R.; Romanelli, G. Hydrotalcites in Organic Synthesis: Multicomponent Reactions. *Curr. Org. Synth.* **2018**, *15*, 1073–1090. [[CrossRef](#)]
42. Cravotto, G.; Cintas, P. Power ultrasound in organic synthesis: Moving cavitation chemistry from academia to innovative and large-scale applications. *Chem. Soc. Rev.* **2006**, *35*, 180–196. [[CrossRef](#)] [[PubMed](#)]
43. Cravotto, G.; Cintas, P. Harnessing mechanochemical effects with ultrasound-induced reactions. *Chem. Sci.* **2012**, *3*, 295–307. [[CrossRef](#)]
44. Lévêque, J.-M.; Cravotto, G. Microwaves, power ultrasound, and ionic liquids. A new synergy in green organic synthesis. *Chimia* **2006**, *60*, 313. [[CrossRef](#)]
45. Tagliapietra, S.; Gaudino, E.C.; Cravotto, G. The use of power ultrasound for organic synthesis in green chemistry. In *Power Ultrasonics*; Elsevier: Amsterdam, The Netherlands; Woodhead Publishing: Sawston, Cambridge, UK, 2015; pp. 997–1022.
46. Martínez, R.F.; Cravotto, G.; Cintas, P. Organic Sonochemistry: A Chemist's Timely Perspective on Mechanisms and Reactivity. *J. Org. Chem.* **2021**, *86*, 13833–13856. [[CrossRef](#)]
47. Lupacchini, M.; Mascitti, A.; Giachi, G.; Tonucci, L.; d'Alessandro, N.; Martínez, J.; Colacino, E. Sonochemistry in non-conventional, green solvents or solvent-free reactions. *Tetrahedron* **2017**, *73*, 609–653. [[CrossRef](#)]
48. Azzena, U.; Carraro, M.; Pisano, L.; Monticelli, S.; Bartolotta, R.; Pace, V. Cyclopentyl methyl ether: An elective ecofriendly ethereal solvent in classical and modern organic chemistry. *ChemSusChem* **2019**, *12*, 40–70. [[CrossRef](#)]
49. de Gonzalo, G.; Alcántara, A.R.; Domínguez de María, P. Cyclopentyl methyl ether (CPME): A versatile eco-friendly solvent for applications in biotechnology and biorefineries. *ChemSusChem* **2019**, *12*, 2083–2097. [[CrossRef](#)]
50. Al-Bogami, A.S.; Saleh, T.S.; Zayed, E.M. Divergent reaction pathways for one-pot, three-component synthesis of novel 4H-pyranol [3, 2-h] quinolines under ultrasound irradiation. *Ultrason. Sonochem.* **2013**, *20*, 1194–1202. [[CrossRef](#)]
51. Mokhtar, M.; Saleh, T.; Ahmed, N.; Al-Thabaiti, S.; Al-Shareef, R. An eco-friendly N-sulfonylation of amines using stable and reusable Zn–Al-hydrotalcite solid base catalyst under ultrasound irradiation. *Ultrason. Sonochem.* **2011**, *18*, 172–176. [[CrossRef](#)]
52. Saleh, T.S.; Al-Bogami, A.S.; Mekky, A.E.; Alkhatlan, H.Z. Sonochemical synthesis of novel pyranol [3, 4-e][1, 3] oxazines: A green protocol. *Ultrason. Sonochem.* **2017**, *36*, 474–480. [[CrossRef](#)] [[PubMed](#)]
53. Ahmed, N.S.; Saleh, T.S.; H El-Mossalamy, E.-S. An efficiently sonochemical synthesis of novel pyrazoles, bipyrazoles and pyrazol-3-ylpyrazolo [3, 4-d] pyrimidines incorporating 1H-benzimidazole Moiety. *Curr. Org. Chem.* **2013**, *17*, 194–202. [[CrossRef](#)]
54. Saleh, T.S.; Eldebs, T.M.; Albishri, H.M. Ultrasound assisted one-pot, three-components synthesis of pyrimido [1, 2-a] benzimidazoles and pyrazolo [3, 4-b] pyridines: A new access via phenylsulfone synthon. *Ultrason. Sonochem.* **2012**, *19*, 49–55. [[CrossRef](#)] [[PubMed](#)]

55. Theiss, F.L.; Ayoko, G.A.; Frost, R.L. Thermogravimetric analysis of selected layered double hydroxides. *J. Therm. Anal. Calorim.* **2013**, *112*, 649–657. [[CrossRef](#)]
56. Puttaswamy, N.; Kamath, P.V. Reversible thermal behaviour of layered double hydroxides: A thermogravimetric study. *J. Mater. Chem.* **1997**, *7*, 1941–1945. [[CrossRef](#)]
57. Theiss, F.L.; Palmer, S.J.; Ayoko, G.A.; Frost, R.L. Sulfate intercalated layered double hydroxides prepared by the reformation effect. *J. Therm. Anal. Calorim.* **2012**, *107*, 1123–1128. [[CrossRef](#)]
58. Nakahira, A.; Kubo, T.; Murase, H. Synthesis of LDH-type clay substituted with Fe and Ni ion for arsenic removal and its application to magnetic separation. *IEEE Trans. Magn.* **2007**, *43*, 2442–2444. [[CrossRef](#)]
59. Guo, Y.; Gong, Z.; Li, C.; Gao, B.; Li, P.; Wang, X.; Zhang, B.; Li, X. Efficient removal of uranium (VI) by 3D hierarchical Mg/Fe-LDH supported nanoscale hydroxyapatite: A synthetic experimental and mechanism studies. *Chem. Eng. J.* **2020**, *392*, 123682. [[CrossRef](#)]
60. Zobon, R.K.; Jassim, T.E. WITHDRAWN: Preparation of Mg-Fe-LDH to study its effectiveness in adsorption of lead from its aqueous solution. *Mater. Today Proc.* **2021**, *05*, 524. [[CrossRef](#)]
61. Sanati, S.; Rezvani, Z. Ultrasound-assisted synthesis of NiFe-layered double hydroxides as efficient electrode materials in supercapacitors. *Ultrason. Sonochem.* **2018**, *48*, 199–206. [[CrossRef](#)]
62. Zubair, M.; Aziz, H.A.; Ahmad, M.A.; Ihsanullah, I.; Al-Harathi, M.A. Adsorption and reusability performance of M-Fe (M = Co, Cu, Zn and Ni) layered double hydroxides for the removal of hazardous Eriochrome Black T dye from different water streams. *J. Water Process Eng.* **2021**, *42*, 102060. [[CrossRef](#)]
63. Guo, Y.; Zhu, Z.; Qiu, Y.; Zhao, J. Synthesis of mesoporous Cu/Mg/Fe layered double hydroxide and its adsorption performance for arsenate in aqueous solutions. *J. Environ. Sci.* **2013**, *25*, 944–953. [[CrossRef](#)]
64. Thommes, M.; Kaneko, K.; Neimark, A.V.; Olivier, J.P.; Rodriguez-Reinoso, F.; Rouquerol, J.; Sing, K.S. Physisorption of gases, with special reference to the evaluation of surface area and pore size distribution (IUPAC Technical Report). *Pure Appl. Chem.* **2015**, *87*, 1051–1069. [[CrossRef](#)]
65. Pérez-Verdejo, A.; Sampieri, A.; Pfeiffer, H.; Ruiz-Reyes, M.; Santamaría, J.-D.; Fetter, G. Nanoporous composites prepared by a combination of SBA-15 with Mg–Al mixed oxides. Water vapor sorption properties. *Beilstein J. Nanotechnol.* **2014**, *5*, 1226–1234. [[CrossRef](#)] [[PubMed](#)]
66. Le, T.A.; Kim, J.; Jeong, Y.R.; Park, E.D. CO₂ Methanation over Ni/Al@MAI₂O₄ (M = Zn, Mg, or Mn) Catalysts. *Catalysts* **2019**, *9*, 599. [[CrossRef](#)]
67. Gupta, P.; Mahajan, A. Green chemistry approaches as sustainable alternatives to conventional strategies in the pharmaceutical industry. *RSC Adv.* **2015**, *5*, 26686–26705. [[CrossRef](#)]
68. Mekky, A.E.; Saleh, T.S.; Al-Bogami, A.S. Synthesis of novel pyrazoles incorporating a phenothiazine moiety: Unambiguous structural characterization of the regioselectivity in the 1, 3-dipolar cycloaddition reaction using 2D HMBC NMR spectroscopy. *Tetrahedron* **2013**, *69*, 6787–6798. [[CrossRef](#)]
69. Prime, R.B.; Bair, H.E.; Vyazovkin, S.; Gallagher, P.K.; Riga, A. *Thermogravimetric Analysis (TGA)*; John Wiley & Sons, Inc.: New York, NY, USA, 2009; pp. 241–317.
70. Bunaciu, A.A.; UdrișTioiu, E.G.; Aboul-Enein, H.Y. Aboul-Enein, X-ray diffraction: Instrumentation and applications. *Crit. Rev. Anal. Chem.* **2015**, *45*, 289–299. [[CrossRef](#)] [[PubMed](#)]
71. Fifield, F.W.; Kealey, D. *Principles and Practice of Analytical Chemistry*; Blackwell Science: Oxford, UK, 2000; p. 324.
72. Webb, P.A.; Orr, C.; Camp, R.; Olivier, J.; Yunes, S. *Analytical Methods in Fine Particle Technology*; Micromeritics Instrument Corporation: Norcross, GA, USA, 1997.
73. Amenomiya, Y.; Cvetanovic, R.J.T.; Chenier, J.H.B. Application of Flash-Desorption Method to Catalyst Studies. IV. Adsorption of Ammonia on Alumina and Its Effect on Adsorption of Ethylene. *J. Phys. Chem.* **1964**, *68*, 52–57. [[CrossRef](#)]
74. Olsen, R.E. Synthesis, Characterization, and Application of High Surface Area, Mesoporous, Stabilized Anatase TiO₂ Catalyst Supports. *Brigh. Young Univ.* **2013**, 3613345, 77–85.
75. Sing, K.J.C. The use of nitrogen adsorption for the characterisation of porous materials. *Physicochem. Eng. Asp.* **2001**, *187*, 3–9. [[CrossRef](#)]
76. Rouquerol, J.; Rouquerol, F.; Llewellyn, P.; Maurin, G.; Sing, K.S. *Adsorption by Powders and Porous Solids: Principles, Methodology and Applications*; Academic Press: Cambridge, MA, USA, 2013; p. 11.
77. Brunauer, S.; Emmett, P.H.; Teller, E. Adsorption of gases in multimolecular layers. *J. Am. Chem. Soc.* **1938**, *60*, 309–319. [[CrossRef](#)]
78. He, Q.; Li, D.; Sun, Q.; Wei, B.; Wang, S. The determination of pore volume and area distributions in porous substances. I. Computations from nitrogen isotherms. *Energy* **1951**, *260*, 125100. [[CrossRef](#)]
79. Batten, S.R.; Duriska, M.B.; Jensen, P.; Lu, J. Synthesis and Complexes of the New Scorpionate Ligand Tris [3-(4-benzonitrile)-pyrazol-1-yl] borate. *Aust. J. Chem.* **2007**, *60*, 72–74. [[CrossRef](#)]
80. Farag, A.M.; Algharib, M.S. Synthesis and reactions of C-(2-thenoyl)-N-arylformhydrazidoyl bromides. *Org. Prep. Proced. Int.* **1988**, *20*, 521–526. [[CrossRef](#)]

Disclaimer/Publisher’s Note: The statements, opinions and data contained in all publications are solely those of the individual author(s) and contributor(s) and not of MDPI and/or the editor(s). MDPI and/or the editor(s) disclaim responsibility for any injury to people or property resulting from any ideas, methods, instructions or products referred to in the content.